3-D Passive Cavitation Imaging Using Adaptive Beamforming and Matrix Array Transducer With Random Apodization

Audrey Sivadon, Francois Varray, Jean-Christophe Béra, Barbara Nicolas, Bruno Gilles

3D passive cavitation imaging using adaptive beamforming and matrix array transducer with random apodization

A. Sivadon, F. Varray, *Member, IEEE*, J.C Béra, B. Nicolas, *Member, IEEE*, B. Gilles

***Abstract*—With the development of promising cavitation-based treatments, the interest in cavitation monitoring with passive acoustic mapping (PAM) is significantly increasing. While most of studies regarding PAM are performed in 2D, 3D imaging modalities are getting more attention relying on either custom-made or commercial matrix probes. Unless specific phased-arrays are used for a specific application, limitations due to probe apertures often results in poor performances of the 3D mapping, due to the use of a Delay-And-Sum (DAS) classic beamformer, which results in strong artifacts and large main lobe sizes. In this paper, 3D-PAM is achieved by performing adaptive beamforming in the frequency domain in 3D, and using a random sparse apodization of a commercial matrix array driving only 256 elements among the 1024 available. It reduces the computation time and makes use of only one 256-channel research platform. Three beamformers have been implemented in 3D and in the Frequency Domain: The DAS beamformer, which corresponds to the beamformer used in previous 3D-PAM studies, the Robust Capon Beamformer (RCB), an adaptive algorithm widely used in 2D-PAM for its high performances, and the MidWay (MW) beamformer, an adaptive algorithm with a computation complexity equivalent to the one of DAS. These algorithms are evaluated both in simulations and experiments with a harmonic source at different positions, and are also applied to real cavitation signals. The results show that, in the case of matrix-arrays of small aperture such as generic commercial matrix probes, the DAS beamformer leads to large main lobe sizes, while adaptive beamformers largely improve the performances of the mapping. The low computation time and its parameter-free character make MW beamformer a good compromise for 3D-PAM applications. It thus appears that a random sparse apodization combined with adaptive beamforming is a good solution to achieve high performance 3D-PAM with manageable devices.**

***Index Terms*—3D Passive Acoustic Mapping, Sparse Array, Adaptive Passive Beamforming, Cavitation, MidWay**

I. Introduction

PASSIVE imaging of cavitation has been of increasing interest for the past decade. The motivation on this method to localize cavitation events yields in the development of cavitation-based promising applications such as drug delivery for cancer treatments [1], disruption of blood clots or cancer tumors with histotripsy [2], [3], or pain reduction [4]. Those therapy modalities have taken advantage of the cavitation dynamics but, due to its complex behaviour, there is still a critical need for cavitation monitoring during the treatment to ensure its safety and efficiency.

Cavitation-based treatments can today be monitored in clinics with either MRI or ultrasound (US) active imaging. MRI guidance offers good resolution and contrast, but is expensive [5]. US active imaging is a technique with a low implementation cost and a rather good image quality, and is widely used for US-based therapy monitoring. The drawback of active US imaging for cavitation monitoring is caused by the High-Intensity Focused Ultrasound (HIFU) beam that dazzles the echographic signal during emission. Only remnants of the cavitation activity is imaged just after the HIFU emission, which does not enable monitoring during pulses [5]–[7]. This limit of active US imaging encouraged investigations using passive US imaging of cavitation emissions, in order to keep a low-cost method together with the ability to monitor cavitation during the US treatment. The classical method to perform such a Passive Acoustic Mapping (PAM) relies on the Delay-And-Sum (DAS) beamformer [8]. It delays the signals received by each transducer according to a test source position, and sums them to estimate the signal emitted from this position. This method is very robust but suffers from large sidelobes and a poor axial resolution in cavitation imaging. Improvements have been achieved through adaptive beamformers like Robust Capon Beamformer (RCB) [9]–[11] or Phase Coherence Factor (PCF) beamformer [12] or through different methods like the Singular-Value Decomposition (SVD) filtering [13]. For now, PAM has been used mainly with linear arrays, which allows localization only in one plane. Hence, cavitation events occurring outside from this plane are missed or misplaced by the monitoring, which explains the need for 3D-PAM development.

3D imaging has already largely been studied in active US imaging. It can be performed using linear probes with mechanical scans or freehand scans with mechanical localizers, or 2D matrix arrays with different shapes [14], [15]. For cavitation imaging, mechanical scans are an unsuitable technique as cavitation events have extremely rapid dynamics and real-time localization would not be conceivable. 2D surface arrays have been successfully used to achieve 3D-PAM of cavitation. Most of studies were realized using custom-built hemispherical or spherically-curved arrays [16]–[21] for transcranial focused therapy and cavitation imaging. Only a few studies used more generic commercial 1024-element matrix array [13], [22].

In all cases, the use of matrix arrays with regularly spaced elements can be limited by the inter-element distance that has to be smaller than one half-wavelength in order to avoid the possible occurrence of grating lobes in the reconstructed images [23], which implies, a priori, a large number of small elements distributed over a surface of small aperture. This is the case for the 1024-element probe (Vermon, France)

with a $0.3\,\mathrm{mm}$ pitch used in [13] and [22], whose width is only $1\,\mathrm{cm}$ and for which either a 1024-channel ultrasound research platform (Digital Phased Array Systems, Fraunhofer IBMT), or four synchronized 256-channel Vantage systems (Verasonics, USA) had to be used. This increases drastically the cost of such monitoring systems and the corresponding numerical cost of the processing to localize the cavitation sources. A solution to reduce the number of active elements is to make use of sparse arrays: In active US imaging, a number of sparse configurations, either optimized or random, has been studied [23], [24], showing the potential of such techniques to provide correct images with a reduced number of elements.

In passive US imaging, sparse configurations were first used in hemispherical sparse arrays [16]–[19]. Using 128-elements randomly distributed over $\simeq 30\,\mathrm{cm}$ diameter hemispherical surfaces covering the human skull, 3D-DAS beamforming algorithms were used to localize cavitation events. Such sparse random apodizations enable to avoid grating lobes in reconstructed images even for large inter-element distances. Thus large aperture arrays can be developed with a reduced number of elements. For such low f-number configurations, the 3D-DAS beamforming algorithm enabled to achieve axial resolutions of a few millimeters.

Nevertheless, such custom-built hemispherical configurations are very specific to transcranial therapy and imaging, and the case of more versatile and generic systems like the above-mentioned commercial array used in [13] and [22] have to be considered. In a preliminary study [25], we compared 3D-PAM of a simulated harmonic point-source computed with a full matrix array similar to this commercial probe, to the one obtained with a random sparse array using only 256 elements among the 1024 available. It confirmed the pertinence of using a spatial apodization which reduces the number of active elements from 1024 to 256 with a random spatial pattern with negligible loss in the image quality and a drastic reduction of the computational cost. Anyway, in the case of such generic probes, working with sparse apodizations does not help with the low aperture of such devices resulting from the spatial sampling constraint. A consequence is that for configurations with f-numbers larger than 1, diffraction effects have a strong influence on DAS-based beamformer performances, leading to poor axial resolution with high levels of artifacts. Lu *et al.* [26] recently managed, in the context of a linear array, to combine signals from different apodizations to enhance the performances of a DAS beamformer, but this enhancement was only in terms of artifact reduction.

The present study aims at implementing adaptive beamformers in 3D to improve PAM performances both in terms of artifact reduction as of resolution enhancement, together with a random sparse apodization allowing the use of one single 256-channel ultrasound research platform, in order to achieve a manageable 3D-PAM with high performances.

The beamformers studied in this paper are Frequency-Domain DAS (FD-DAS), Frequency-Domain RCB (FD-RCB) and Frequency-Domain MidWay (FD-MW). FD-DAS is the non-adaptive beamformer classically used for now for 3D-PAM. Concerning adaptive beamforming, RCB is widely used in 2D-PAM for its good image quality, and we implement here a Frequency-Domain version of the algorithm introduced in [27]. As for FD-MW, it is a particular case of the Pisarenko class of beamformers [10] and has the advantage of presenting a low numerical complexity comparable to FD-DAS. To evaluate the proposed method, we first present simulations of harmonic point-sources beamformed using all three algorithms, with a comparison between the full and random sparse arrays. For an experimental validation, imaging of a compact scatterer acting as a harmonic point-like source as well as cavitation imaging are performed using the random sparse array and all three beamformers.

II. Method

A. General mathematical formulation

In this paper, PAM is performed in the Frequency Domain (FD) using the Cross-Spectral Matrix (CSM) formulation and its robust estimation [28], [29]. As shown in [27], this formulation enables an easy adaptation of existing beamformers to the context of PAM, to localize cavitation sources. Considering an N-element array, the expression of the estimated CSM is [27]:

$$\hat{\mathbf{M}}(f) = \frac{1}{K}\sum_{k=1}^{K}\frac{1}{T_{snap}}\mathbf{Y}_k(f)\mathbf{Y}_k^*(f). \tag{1}$$

In this expression, the entire recorded signal of duration T_{rec} has been segmented into K successive and partially overlapping snapshots of duration T_{snap}, that represent K artificial realizations of the acquisition over which the CSM estimation is performed. $\mathbf{Y}_k(f)$, a $1\times N$ vector, is the Fourier transform at the frequency f of the received signals for the realization k on each element of the array. For a matrix array, the N elements are numbered in an arbitrary order, and the $\mathbf{Y}_k(f)$ matrix is of dimensions $1\times N$ whatever the type of probe used, the CSM being thus an $N\times N$ matrix. $[.]^*$ represents the complex conjugate.

The CSM is used to analyze the degree of correlation between signals received by each couple of transducers. The main advantage of this formulation is that the CSM does not depend on the pixel positions; Hence this matrix can be computed only once and then used on any imaging grids. This allows for saving computation time, compared to the time domain formulation of the corresponding beamformers, for which the cross-correlation matrix needs to be evaluated for each pixel position, which becomes a critical aspect for 3D-PAM.

To recover the source position, the mean power spectral density $\hat{P}(\mathbf{r},f)$ is expressed:

$$\hat{P}(\mathbf{r},f) = \mathbf{h}^*(\mathbf{r},f)\hat{\mathbf{M}}(f)\mathbf{h}(\mathbf{r},f). \tag{2}$$

with $\mathbf{h}(\mathbf{r},f)$, the steering vector which points a pixel position $\mathbf{r}$ included in an arbitrary imaging grid. Let us notice that the size of $\hat{P}(\mathbf{r},f)$ depends only on the dimensions of the reconstructed imaging grid. Using a matrix array allows to map a third dimension, so that the sizes of the reconstructed map can be set by the user to $N_x\times N_y\times N_z$ were N_x, N_y

and N_z are the number of pixels in the x, y and z directions, respectively.

The quality of the reconstructed power maps relies on the values of the parameters K and T_{snaps} of the robust estimation of the CSM, which are directly linked as follows:

$$K = \frac{T_{rec}}{(1 - p_{overlap})T_{snap}} \tag{3}$$

where T_{rec} is the duration of the entire recorded signal and $p_{overlap}$ is the percentage of overlapping signal between two artificial realizations, which allows for higher values of K for a given value of T_{snap}. Indeed, without overlapping, increasing the parameter K allows a better estimation of the CSM, but with the drawback of reducing the value of T_{snap} which can limit the resolution of Fourier transform of the partitioned signals.

In this paper, we propose to use the estimation of the CSM formulation in the frequency domain to provide adaptive as well as non-adaptive 3D beamforming. The beamformers will then be named FD-beamformer, for Frequency Domain.

B. Non-adaptive FD-DAS beamformer

For the non-adaptive FD-DAS beamformer, the power is computed using equation (2) with:

$$\begin{cases} \mathbf{h}_{FD_{DAS}}(\mathbf{r}, f) & = \dfrac{\mathbf{a}(\mathbf{r}, f)}{N} \\ \hat{P}_{FD_{DAS}}(\mathbf{r}, f) & = \dfrac{\mathbf{a}^*(\mathbf{r}, f)\hat{\mathbf{M}}(f)\mathbf{a}(\mathbf{r}, f)}{N^2}, \end{cases} \tag{4}$$

where $\mathbf{a}(\mathbf{r}, f)$ is the propagation vector that will be further discussed in Section II-E. FD-DAS is the frequency domain equivalent of the beamformer used for 3D-PAM in the literature [18], [20], [30]. The low complexity of the algorithm makes it more interesting for real-time monitoring applications but at the cost of large artifacts and of a broad Point Spread Function (PSF) especially in the axial direction (here along z). This lack of precision in the source localization is the motivation for going to adaptive beamformers, especially in the context of 3D beamforming where the aperture of the probe is small.

C. Adaptive FD-RCB beamformer

Robust Capon Beamformer is an adaptive beamformer used in the medical US literature in the time domain [9]–[11], [31] and has recently been transposed to the frequency domain [27] with the CSM formulation. It is derived from the Capon beamformer, which obtains an expression of the steering vector by minimizing the power of any type of noise, but which is practically unusable because of a very unstable behavior in the presence of model errors [9]. The resolution of the RCB problem considers that, in presence of error models, the optimal propagation vector $\hat{\mathbf{a}}_\mathbf{0}(\mathbf{r}, f)$ has to be found close to the propagation vector $\mathbf{a}(\mathbf{r}, f)$, the difference between them being controlled by the parameter ϵ such that $||\hat{\mathbf{a}}_0(\mathbf{r}, f) - \mathbf{a}(\mathbf{r}, f)||^2 \leq \epsilon$. The minimization problem is then directly formulated in terms of $\hat{\mathbf{a}}_\mathbf{0}(\mathbf{r}, f)$ instead of the steering vector, and the power density finally reads [27]:

$$\begin{cases} \hat{\mathbf{a}}_0(\mathbf{r}, f) & = \mathbf{a}(\mathbf{r}, f) - \left(\mathbf{I} + \lambda(\epsilon)\hat{\mathbf{M}}(f)\right)^{-1} \mathbf{a}(\mathbf{r}, f), \\ \hat{P}_{FD_{RCB}}(\mathbf{r}, f) & = \dfrac{||\hat{\mathbf{a}}_0(\mathbf{r}, f)||^2/N}{\hat{\mathbf{a}}_0^*(\mathbf{r}, f)\hat{\mathbf{M}}^{-1}(f)\hat{\mathbf{a}}_0(\mathbf{r}, f)}. \end{cases} \tag{5}$$

where $\mathbf{I}$ is the identity matrix and $\lambda(\epsilon)$ is the Lagrange multiplier resulting from a Newton-Raphson numerical method to find an optimal value for each pixel, controlled by the ϵ parameter.

FD-RCB appears as a more complex beamformer, as for each pixel an optimization computation is performed. This method implies a matrix inversion of the CSM resulting in the $K > N$ condition for the number of realizations in the estimation of equation (1). This complexity results in a significantly smaller PSF than for FD-DAS and considerably reduced artifacts with the drawback of an important time computation. The numerical cost is a critical aspect, especially in 3D imaging, where the computation of the CSM is increased because of the amount of acquired data and of the power map computation which is done on a volumetric imaging grid.

D. Adaptive FD-MW beamformer

As an alternative to FD-RCB, another adaptive algorithm is studied, further denoted as the Frequency Domain MidWay (FD-MW) beamformer. It is a particular case of the Pisarenko class of beamformers [27], [32], [33]. The Pisarenko class of beamformers uses the CSM raised to the power r to compress level differences between sources before steering computation [27] where the value of the power r can be chosen in the range $[-1; 1]$. The extreme cases of the Pisarenko class correspond, on the one side to the FD-DAS beamformer ($r = 1$), on the other side to the Capon beamformer ($r = -1$). Both methods have their own drawbacks: Broad PSF and large artifacts for FD-DAS, lack of robustness against error models and instability for Capon. Stoica *et al.* have pointed out the relevance of using the limit $r \to 0$, denoted the MidWay case, leading to the following formulation [27], [32]:

$$\begin{cases} h_{FD_{MW}}(\mathbf{r}, f) & = \dfrac{\mathbf{a}(\mathbf{r}, f)}{\sqrt{N}} \\ \hat{P}_{FD_{MW}}(\mathbf{r}, f) & = \exp[\mathbf{h}^* \ln(\hat{\mathbf{M}})\mathbf{h}] \end{cases}, \tag{6}$$

where the expression of $\hat{P}_{FD_{MW}}(\mathbf{r}, f)$ can be deduced from the $r \neq 0$ case of equation (20) in [32] by taking the first order Taylor expansion of $\hat{\mathbf{M}}^r$ at $r = 0$.

In 2D passive imaging, the FD-MW beamformer has been proven to give well-balanced performances between DAS and RCB, thanks to a computation complexity equivalent to the one of FD-DAS, for metrics approaching performances of FD-RCB [34]. This allows to propose FD-MW as a good compromise between previously presented beamformers, in the context of 3D-PAM.

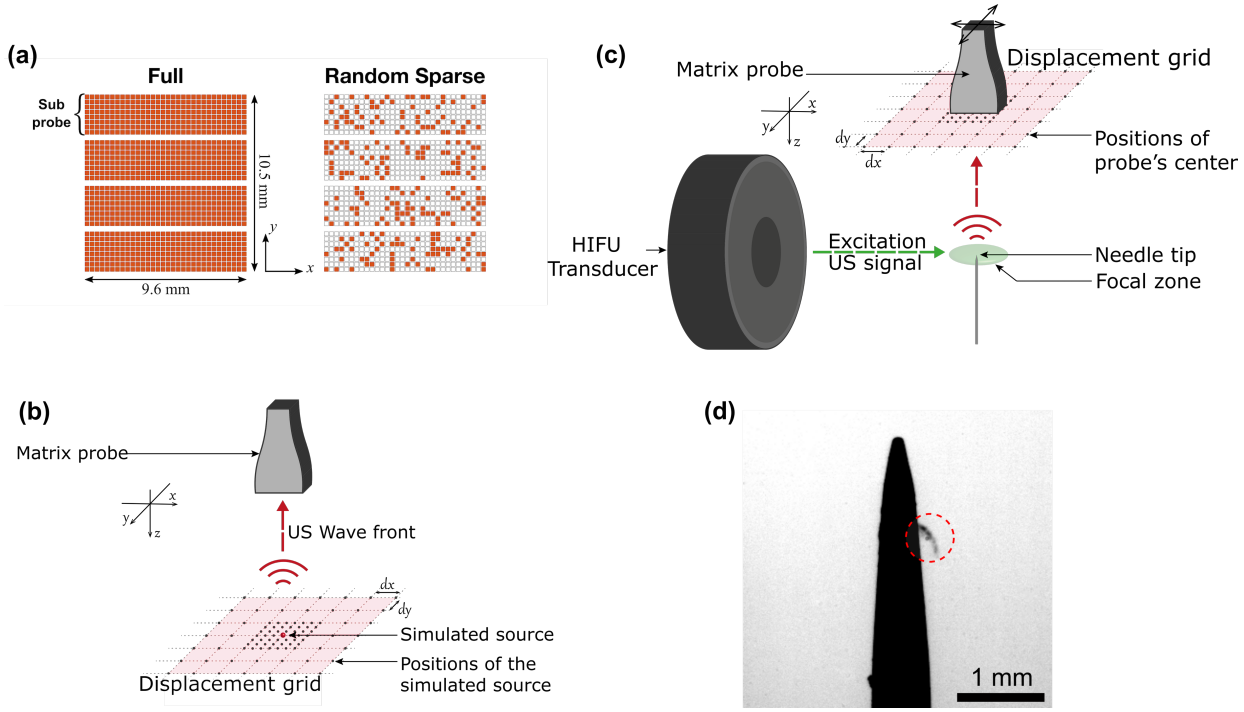

Fig. 1: **Simulated and Experimental Configurations.** (a) Representation of the matrix array on the (x, y) plane for the full (left) and a random sparse (right) apodization used in this paper, with red filled squares and empty squares representing the active and inactive elements of the array respectively. (b) Representation of the simulations with a simulated source (red spot) positioned at $(0, 0, 20)\,\mathrm{mm}$. The source will be positioned successively on each point of the black spot grid on the red plane at $z = 20\,\mathrm{mm}$. The $(0, 0, 0)$ of the coordinate system is placed at the center of the probe. The grid has a spacing of $dx = dy = 5\,\mathrm{mm}$, with a denser central part of width $10\,\mathrm{mm}$ (corresponding to the probe footprint) in which grid spacing is reduced to $1.67\,\mathrm{mm}$. (c) Representation of the experimental setup with a compact scatterer (a needle tip) placed at the focal point of a HIFU transducer. The acoustic direction of the excitation beam is on the x axis. In this experimental setup, the scattering source is fixed, and the probe center is moved along the nodes of a grid identical to the one of (b), to mimic the displacement of the scattering source in the coordinate system of the array. The center of this grid is $20.7\,\mathrm{mm}$ above the source. (d) Optical image of the needle tip during cavitation experiment. The diameter of the needle at the bottom of the image is $0.7\,\mathrm{mm}$, and a typical bubble cloud nucleated at the needle surface can be seen in the dotted circle (the HIFU transducer is on the left). The needle is the same as the one used in (c).

E. 3D formulation

Using the CSM formulation, 3D-PAM is directly implemented through the expressions of the propagation vector $\mathbf{a}(\mathbf{r}, f)$ for each of the beamformers, expressed as:

$$a_n(\mathbf{r}, f) = \exp\left(-i2\pi f \frac{||\mathbf{r_n} - \mathbf{r}||}{c}\right), \tag{7}$$

where c represents the sound speed and $\mathbf{r}_n$ the 3D positions of the N elements of the array in the 3D space. The values of $\mathbf{r}_n$ depend on the array type: For a matrix array as considered in this paper, z_n equals 0, while one would write $y_n = z_n = 0$ for a linear array.

Using a full matrix array implies the use of a high number of elements. The method of random sparse apodization enables to reduce the number of active elements from 1024 to 256, for example with a random pattern covering the whole probe surface (see Fig. 1), which allows using only one 256-channel ultrasound research platform, and a strong reduction of the computational cost. Configurations with 128 and 64 active elements randomly distributed over the whole probe surface are also tested in this study. The quality of the power maps thus obtained will be compared to full probe mapping using simulated data.

III. Materials

A. Matrix Array and Random Apodization

The matrix array used in this study is a $3\,\mathrm{MHz}$ matrix probe (Vermon, France) of 1024 sensors arranged as shown in Fig. 1 with 32 elements along the x and y directions. The pitch is $0.300\,\mathrm{mm}$, with element that are $0.275\,\mathrm{mm}$ wide, so that the whole matrix size is $9.6 \times 10.5\,\mathrm{mm}$ (see below for the reason of the small asymmetry). The length of the diagonal of the array will be further denoted $2D$. The center frequency of the probe is $3.4\,\mathrm{MHz}$ and its bandwidth at -6 dB ranges from $2.4\,\mathrm{MHz}$ to $4.5\,\mathrm{MHz}$. Simulations are done by considering elements as point-like receivers, with either an array identical to the full probe of 1024 active sensors, or a random sparse probe consisting of a set of 256, 128 or 64 active elements placed randomly on the array. The random sparse apodizations are experimentally obtained using

a Universal Transducer Adapter UTA 1024-MUX (Verasonics, USA), which imposes a technical constraint on the choice of the active elements. Indeed, the array is divided into 4 sets of 32×8 elements causing a small asymmetry (Fig. 1), and each element with the same position on each sub-probe are wired together. Thus, only one of the 4 elements wired together can be chosen for the random sparse array. This constraint ensures that the active elements are distributed over the whole probe aperture, and a similar rule has been applied to all simulated random sparse apodizations.

B. Simulations

To evaluate the performances of 3D passive imaging coupled with random apodization, a point source is simulated at different positions corresponding to the nodes of the grid shown in Fig. 1. This grid is a $30\,\mathrm{mm}$ square, with $5\,\mathrm{mm}$ spacing between nodes, and including an inner denser part which corresponds to the probe's footprint. This inner denser part is a $10\,\mathrm{mm}$ square, in which node spacing is reduced to $1.67\,\mathrm{mm}$. The grid is placed at a depth of $20\,\mathrm{mm}$ from the probe.

The simulated source is a $2\,\mathrm{MHz}$ sinusoidal source with a $20\,\mathrm{ms}$ pulse duration. A white Gaussian noise has been added to simulate an acquisition noise with a $10\,\mathrm{dB}$ Signal to Noise Ratio (SNR) over the whole bandwidth of the probe. Each node of the grid is processed as an independent simulation and the source signal is propagated at $1480\,\mathrm{m/s}$ to each element of the matrix array to simulate the acquisition. To ensure and confirm the pertinence of the random sparse apodization, the simulations have been done with both the full and the random sparse probes.

In addition to this single source main configuration, one simulation is also performed with point sources on all grid nodes emitting simultaneously, in order to illustrate how the single-source results obtained for those beamformers compare to an equivalent multi-source emission configuration. For that configuration, a limitation common to all TEA-based beamformers implies that there is no coherence between sources [35]. For that reason, wideband random noise emission is being used here for each source, with a $20\,\mathrm{ms}$ pulse duration, instead of sinusoidal emission. As in the single source configuration, a white Gaussian noise has been added to simulate an acquisition noise with a $10\,\mathrm{dB}$ Signal to Noise Ratio (SNR) over the whole bandwidth of the probe. For this simulation, only a random sparse apodization is used.

C. Experiments

For all experiments presented below the random sparse array is used.

a) Harmonic compact scatterer imaging: A first experimental set-up aims at characterizing the ability of the matrix array with random apodization, to localize a scattering point-like source (without cavitation), using above-mentioned non-adaptive and adaptive beamformers. For that purpose, the tip of a needle placed at the focus of a HIFU transducer is used as a compact scatterer acting as a small source for the passive imaging (Fig. 1). The diameter of the needle in its central part is $0.7\,\mathrm{mm}$, and the sonicated region at the tip of the needle is everywhere less than $0.5\,\mathrm{mm}$ in diameter. The HIFU transducer is a $1\,\mathrm{MHz}$ spherical transducer focused at $8\,\mathrm{cm}$ with a diameter of $10\,\mathrm{cm}$ and a circular aperture of $4.5\,\mathrm{cm}$ in diameter in the center (Imasonic, France). Its focal zone at $-3\,\mathrm{dB}$ is an ellipsoidal shape of $8.3\,\mathrm{mm}$ along the x axis and $1.1\,\mathrm{mm}$ along the y and z axis. An ultrasound beam is emitted by the HIFU transducer using a signal generator and a power amplifier (GN1000; PRÂNA, France): Sinusoidal bursts of $20\,\mathrm{ms}$ at frequency $1\,\mathrm{MHz}$ are emitted. The signal scattered by the tip of the needle is passively acquired by the matrix array using a 256-channel Vantage System (Verasonics, USA) with the UTA multiplexer. The whole set-up is immersed in a filtered water tank. Experiments are performed using two amplitudes to evaluate the influence of SNR on the performances of every beamformer. The SNR is obtained by evaluating the noise power using a pre-acquisition made just before the emission of the HIFU signal and the power of the signal part simply defined as the difference between the total power of the acquired signal and the noise power. The low amplitude configuration corresponds to a peak pressure amplitude at the focus of $0.6\,\mathrm{MPa}$ and leads to an average SNR of $2.7\,\mathrm{dB}$ for the scattered signals acquired by the probe with sources in the dense grid, while the higher amplitude configuration corresponds to a peak pressure amplitude at the focus of $2.2\,\mathrm{MPa}$ leading to an average SNR on the dense grid of $10\,\mathrm{dB}$. It has to be noted that both amplitudes have been chosen to avoid cavitation in the medium and at the needle tip. Nevertheless, one cavitation event occurred with the higher amplitude series at position $(1.67, -1.67)\,\mathrm{mm}$ of the displacement grid, so that this point has been removed from the analysis.

b) Imaging sequence: To reproduce the same configurations as in simulations regarding the relative positions of the source and the probe, the matrix array is placed at $z = 20\,\mathrm{mm}$ above the needle tip and moved along the x and y axis according to the same displacement grid with a motorized positioning system controlled by the Vantage system, as shown in Fig. 1. The acquisition cycle consists of the following steps: The probe is placed on one node of the displacement grid, and an active imaging sequence with a set of diverging waves is acquired to obtain the Ground Truth (GT). Then, the excitation pulse is triggered, and a passive acquisition sequence at a sampling frequency of $13.8\,\mathrm{MHz}$ is performed during emission. The active imaging acquisitions are post-processed using a DAS compounding algorithm. The positions of the needle tip are extracted and used to calibrate the alignment of the positioning system. It has to be noted that this is done only for nodes of the inner dense grid because of the degradation of the performances of active imaging beyond the probe footprint. On the basis of this calibration, GT is given over the whole displacement grid by the motorized positioning system displacements. The passive acquisitions on all the nodes of the displacement grid are post-processed using the three beamformers FD-DAS, FD-MW and FD-RCB. Further details of their implementation are given in Section III-D.

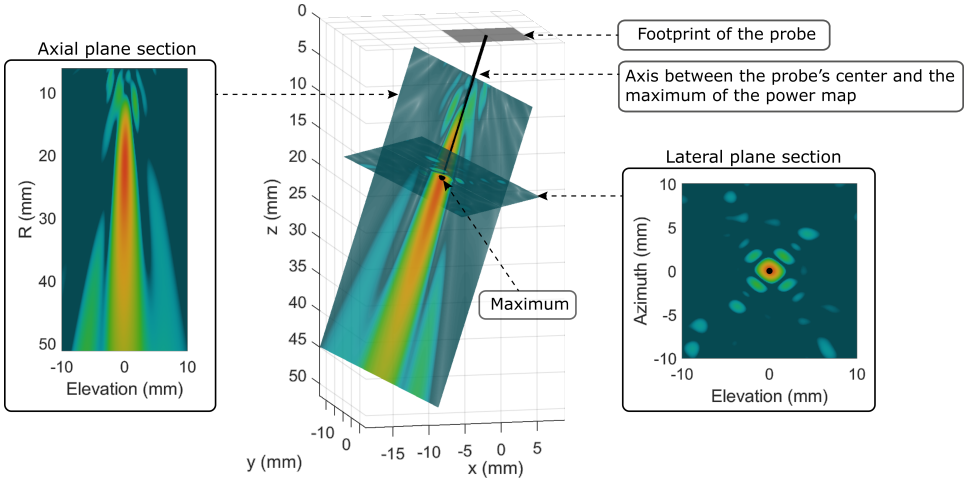

Fig. 2: 3D power map using FD-DAS of a simulated harmonic point source positioned at $(-5, -5, 20)\,\mathrm{mm}$. The reconstructed frequency matches the source frequency, at $2\,\mathrm{MHz}$. The axial and lateral plane sections are obtained using spherical coordinates centered on the probe center.

c) Cavitation imaging: A second set of experiments aiming at localizing a cavitating source has been performed. For that purpose, the needle tip is used as a cavitation catalyzer. To force cavitation events to occur on the needle tip, it has been previously slightly scratched on a paraffin bloc, a hydrophobic material, used here to capture cavitation nuclei at the tip. The HIFU beam is emitting the same sinusoidal burst with a peak pressure amplitude at the focus of $1.8\,\mathrm{MPa}$, sufficient to trigger cavitation on the needle due to the above-mentioned preparation procedure. The imaging sequence is equivalent to the previous set-up with only one off-axis matrix probe position in the dense grid, at position $(3.33, -1.67)\,\mathrm{mm}$. The cavitation activity was confirmed by high frame-rate video recording using ombroscopy with a high-speed camera (Phantom V12.1; Vision Research Inc., USA). A typical image of the needle tip with a bubble cloud is shown in Fig. 1. According to optical images, the bubble cloud sizes obtained for this set of experiments were always $0.5\,\mathrm{mm}$ at most.

D. Reconstruction parameters and metrics

a) Passive imaging parameters: Given the total duration T_{rec} of the recorded signals, the strategy adopted to choose the parameters of the CSM estimation has been discussed in [27]. It is governed by the condition $K > N$ required for the CSM inversion appearing in the RCB algorithm. Considering the equation (3), K is taken close to N to keep T_{snap} as high as possible in order to ensure the best possible frequency resolution. To further increase T_{snap}, $p_{overlap}$ is taken as high as possible but not beyond 90%, to avoid a too high correlation level between the resulting artificial realizations, leading to a degraded quality of the estimation of $\hat{\mathbf{M}}(f)$. The parameters finally chosen for the estimation of the CSM are $K = 260$ and $p_{overlap} = 90\%$ resulting in a snapshot duration of $T_{snap} = 0.78\,\mathrm{ms}$, which corresponds to ~ 1500 periods of the lowest reconstruction frequency used in this study. For the harmonic point-source imaging, the reconstruction frequency is set to $2\,\mathrm{MHz}$. In simulations it is the signal frequency, and in experiments it corresponds to the harmonic with the highest amplitude in the probe bandwidth. It has to be noted that the presence of harmonics, in that case, is only due to the nonlinear propagation of the HIFU beam before scattering by the needle tip. For cavitation imaging, shorter recording times of $T_{rec} = 1.9\,\mathrm{ms}$ are considered, with the same K and $p_{overlap}$ values, which leads to $T_{snap} = 0.073\,\mathrm{ms}$, corresponding to ~ 150 periods of the lowest reconstruction frequency. Three reconstruction frequencies were computed: One harmonic frequency ($2\,\mathrm{MHz}$), one ultra-harmonic frequency ($3.5\,\mathrm{MHz}$), and one frequency representative of wideband noise characteristic of inertial cavitation activity ($4.7\,\mathrm{MHz}$). For each reconstruction frequency, a single frequency bin of $20\,\mathrm{kHz}$ bandwidth was used. Reconstruction of 3D-PAM of cavitation are performed using beamformers detailed in Section II.

For RCB the ϵ value is optimized in the following manner. For each case (simulation or experiment), 3 points of the dense grid are processed: One point on the diagonal $(-5, 5)$, one on the edge of the dense grid $(-5, 0)$, and one at its center $(0, 0)$. The ϵ chosen for the whole grid is the average of the values that minimize the size of the Point Spread Function (PSF) for each of the 3 points. The final values are $\epsilon_{simu} = 0.1$ for simulated data, and $\epsilon_{exp} = 20$ for experimental data. The large difference between ϵ_{simu} and ϵ_{exp} is caused by the experimental conditions, which includes calibration errors on the matrix array and a higher noise level.

To quantify the performances both in simulations and in experiments, several metrics have been selected and are detailed below. In addition to these metrics, the running time for the reconstruction of some of the maps discussed in Section IV has been provided to compare computation times associated to each method. The reconstructions have been carried on a computer using Matlab (R2019b, The MathWorks, Natick, MA, USA), with an Intel(R) Core(TM) i7-8665 CPU at 2.11GHz, and 16GB memory. It has to be kept in mind that this only gives rough indications of the running time performances of each method, since code optimization or

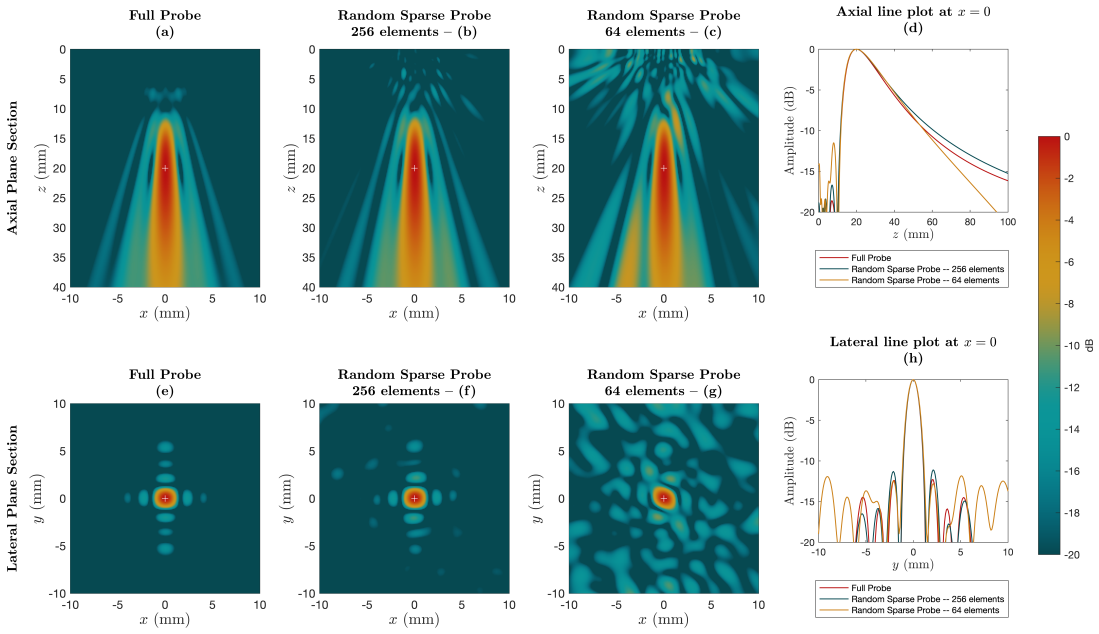

Fig. 3: PAM with FD-DAS algorithm on a simulated source emitting at $2\,\mathrm{MHz}$, placed at $(0, 0, 20)\,\mathrm{mm}$ (white cross) with the top row representing the (x, z) plane for $y = 0$ and the bottom row the (x, y) plane for $z = 20\,\mathrm{mm}$. For each plane, a slice of the reconstructed volume is represented for the full probe and for two examples of random sparse probe with respectively 256 and 64 active elements. The fourth column shows the line plots along the $x = 0$ axis of the corresponding sections for all three apodizations. Note that x, y and z directions are used here since they coincide with elevation, azimuth and axial directions, for a source vertically below the center of the probe.

parallelization could largely modify the results for this aspect.

b) Metrics: The first metric provided is the position error which corresponds to the distance between the reference position of the source and the position of the maximum of the power map. In simulations, the reference position corresponds exactly to the node position on the grid in Fig. 1. In experiments, reference positions are given by the motorized positioning system displacements, after calibration using US active imaging in the dense grid of Fig. 1 (see Section III-C).

As a comparison to the metrics used in 2D-PAM, axial and lateral Full Width at Half Maximum (FWHM) are also provided. They correspond to the FWHM in the axial and lateral directions. To recover the right values, the tilt of the main lobe is taken into account. Indeed, when an angle is applied to the axis between the center of the probe and the source position, the main lobe undergoes a rotation depending on that angle as can be seen in Fig. 2. For that purpose, the position of the maximum is projected in a spherical coordinate basis. The axial plane section corresponds to the R – elevation plane and the lateral plane section corresponds to the elevation – azimuth plane. The azimuth angle on the axial plane is chosen arbitrarily. The axial FWHM corresponds to the size of the portion of the R axis for which the axial power density reaches $-3\,\mathrm{dB}$ from the maximum value of the axial power map. The lateral FWHM is recovered using an ellipsoidal fit in the elevation – azimuth section, and the value recorded is the one corresponding to the longest length at $-3\,\mathrm{dB}$.

The Peak Sidelobe Ratio (PSLR) and the image signal-to-noise ratio (imSNR) defined in [16] are also provided. The PSLR is the ratio of the intensity of the main sidelobe in the reconstructed volume to the main lobe intensity. The imSNR is defined as the ratio of the main lobe intensity to the standard deviation of the pixels whose distance to the main lobe is larger than a wavelength. Since it takes very different values depending on the orientation of the reconstructed maps, values are provided both for axial and lateral planes.

IV. Results

A. Simulations - Comparison between the full probe and the random sparse probe

Fig. 3 presents sections of the reconstructed 3D power map of a simulated source placed at $(0, 0, 20)\,\mathrm{mm}$, using FD-DAS algorithm for both the full (Fig. 3.(a, e)) and for two examples of random sparse probe with respectively 256 and 64 active elements (Fig. 3.(b,f) and (c,g)). For all three apodizations, the axial plane section (Fig. 3.(a, b, c)) and lateral plane section (Fig. 3.(d, e, f)) are shown. The full probe shows a typical PAM reconstruction with a larger size of the main lobe in the axial z direction than in the lateral x and y directions, and very typical diffraction sidelobes in the lateral plane section. The small asymmetry of the matrix array due to the sub-probe wiring mentioned in Section III-A can be seen on the lobe pattern in the lateral plane section.

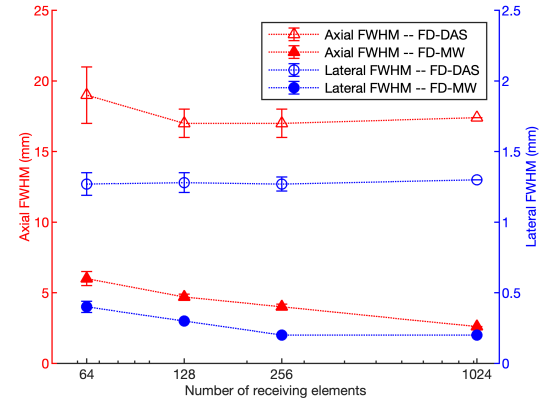

(a)

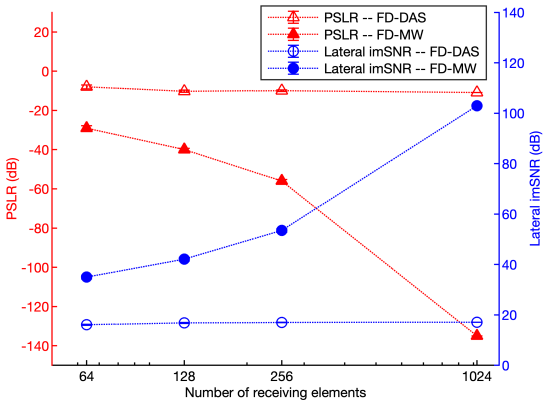

(b)

Fig. 4: [Simulations] (a) Axial and Lateral FWHM and (b) PSLR and Lateral imSNR, for FD-DAS and FD-MW beamformers with source at position $(0, 0, 20)\,\mathrm{mm}$ emitting at $2\,\mathrm{MHz}$, as a function of the number of active elements in apodization. For each random sparse apodization, results are shown as mean values and standard deviations over 10 different apodizations.

Using 256 elements of the matrix array with a random distribution results in power maps very similar to the ones obtained with the full probe. The line plots at $x = 0$ along the z-axis (Fig. 3.d) and y-axis (Fig. 3.h) show that the dimensions of the main lobe is unchanged until a level of $-3\,\mathrm{dB}$ and $-10\,\mathrm{dB}$ for the axial (z) and lateral (y) directions, respectively. Also, the random distribution causes an irregularity in the secondary lobe amplitudes and sizes, which increases the background noise level as revealed by the presence of irregular spots on the lateral plane section with the random sparse probe (Fig. 3). For the 64 element apodization, while the main lobe dimensions at $-3\,\mathrm{dB}$ are only marginally changed, a number of secondary lobes of irregular positions and amplitudes appear, several of them exceeding a level of $-10\,\mathrm{dB}$. Fig. 4 shows the evolution of the metrics as a function of the number of active elements in the apodizations. For random sparse apodizations, simulations have been done for a set of 10 different apodizations for each number of active elements, and are shown in terms of mean values and standard deviations over each set of simulations. For FD-DAS, despite the direct observations discussed above on Fig. 3, reducing the number of active elements only marginally decreases the metrics themselves, except for the axial FWHM with 64 element apodizations. For an adaptive beamformer like FD-MW, which offers better metrics, the degradation is more pronounced. Concerning the standard deviations for a set of random apodizations with the same number of active elements, they are very small in comparison to the mean values of the metrics for PSLR and imSNR, and exceed 10% of the mean value only for the axial FWHM of the FD-DAS beamformer with the 64 element apodization. The 256 element random apodization, being the one that enables the use of a single 256-channel ultrasound research platform with metrics closest to the ones of the full probe, will be the one selected for the rest of the study.

Results presented in the next section (see Table I) give further quantitative details enabling to compare full probe and random sparse probe configurations, showing that both apodizations give maps with very similar metrics.

Regarding computation times, for the axial plane section maps (Fig. 3.(a, b)) both composed of 201201 pixels, they are respectively of $28\,\mathrm{s}$ for the full 1024-element matrix array and $3.4\,\mathrm{s}$ for the sparse 256-element probe. For the lateral plane sections, composed of 40401 pixels, they are respectively of $5.6\,\mathrm{s}$ for the full probe (Fig. 3.(d)) and $0.55\,\mathrm{s}$ for the sparse probe (Fig. 3.(e)). Computation times with the 256-element matrix array are thus 8 to 10 times lower than with the full 1024-element one.

Since power maps obtained with both apodizations reveal very similar features, the following results will only be provided for the random sparse apodization, unless explicitly specified.

B. Simulations - Influence of the position of the source

Fig. 5.(a) collates sections, in the plane $z = 20\,\mathrm{mm}$, of the $-6\,\mathrm{dB}$ main lobes of power maps reconstructed for one simulated source successively placed at every node of the grid with the FD-DAS beamformer. Each lobe is well centered on its reference position, the position of the corresponding node which is perfectly known in the case of simulated data. In that case, the position error is simply defined as the distance between the position of the maximum of a reconstructed volume and the source position at the node. For any node of the displacement grid, it is lower than $0.1\,\mathrm{mm}$, which is the resolution of the reconstructed maps, regardless of the beamformer used.

Lobe section sizes increase with the distance to the center of the grid, revealing both an increase of the whole volume of the main lobe and its tilt in relation to the vertical z direction. The evolution of the FWHM is presented on Fig. 6, as a function of ρ, the distance between a given source and the node $(0, 0, 20)\,\mathrm{mm}$, which is the projection of the probe center on the displacement grid. Results are provided for the three beamformers using signals from the random sparse apodization, and using the full probe for FD-DAS only. An overview of the results is given in Table I, in terms of

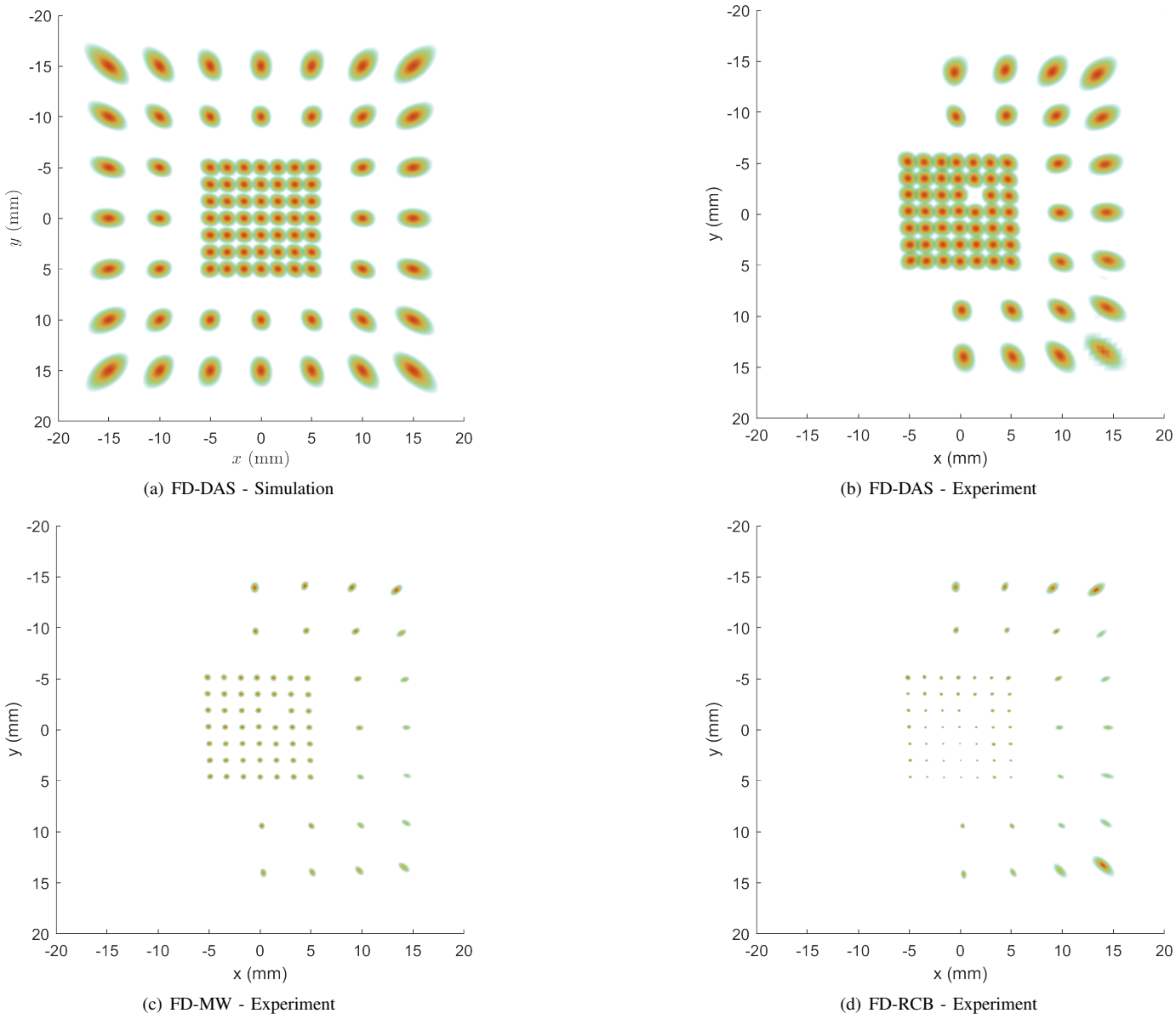

(a) FD-DAS - Simulation

(b) FD-DAS - Experiment

(c) FD-MW - Experiment

(d) FD-RCB - Experiment

Fig. 5: For every position of the source, sections of the $-6\,\mathrm{dB}$ main lobe at a constant depth of (a) $20\,\mathrm{mm}$ for simulations with FD-DAS beamformer (source emitting at $2\,\mathrm{MHz}$ – reconstruction frequency: $2\,\mathrm{MHz}$), and (b-d) $20.7\,\mathrm{mm}$ for experiments (SNR $= 10\,\mathrm{dB}$) with FD-DAS, FD-MW and FD-RCB beamformers, respectively (source: scattered signal at focus of a $1\,\mathrm{MHz}$ HIFU beam – reconstruction frequency: $2\,\mathrm{MHz}$). Random sparse configuration is used in all cases. Let us notice that the point at position $(1.67, -1.67)\,\mathrm{mm}$ is ignored in the experimental results because of a cavitation occurrence unrelevant for this particular study (see Section III-C). Also, the experimental points of the external grid with $x < 0$ are not shown because of direct emission from the HIFU transducer (see Section IV-C).

mean values and standard deviations of the metrics in the dense grid (i.e. the probe footprint). Regarding beamformer performances, as expected, axial FWHM is larger than lateral FWHM, with roughly a factor between both metrics of about 10 for FD-DAS and FD-MW, and 5 for FD-RCB ($\epsilon = 0.1$). As for the evolution of the metrics along the grid, it follows a slight increase in the dense grid and increases more steeply when moving away from the center for all algorithms. For axial FWHM with FD-DAS beamformer, for example, the increase between $\rho = 0$ and $\rho = D$ is only $+25\%$, while it reaches $+360\%$ for the most outlying nodes. This different behavior between the probe footprint and the external part of the displacement grid is even more pronounced for the lateral FWHM.

For the FD-DAS beamformer, results from the simulation with the full probe are also shown in Fig. 6 to complete the comparison with the sparse random apodization. The evolution of the mean values of the metrics is the same in both cases. The difference rather lies in a slightly larger dispersion of the lobe sizes at a given ρ value for the random sparse probe, in

	Axial FWHM (mm)	Lateral FWHM (mm)	PSLR (dB)	Axial imSNR (dB)	Lateral imSNR (dB)
			Dense grid		
FD-DAS - Full	19 (1)	1.4 (0.1)	−11 (1)	10.5 (0.2)	16.6 (0.3)
FD-DAS - Rand	20 (1)	1.4 (0.1)	−10 (1)	10.3 (0.2)	16.6 (0.3)
FD-MW - Rand	3.8 (0.2)	0.3 (0.1)	−75 (2)	18.5 (0.2)	63 (2)
FD-RCB - Rand	0.4 (0.1)	0.1 (0.1)	< -100	> 100	> 100

TABLE I: [Simulations] FWHM and imSNR in the axial and lateral directions as well as PSLR in the dense grid. The values account for FD-DAS with the full probe (Full) and FD-DAS, FD-MW and FD-RCB with the random sparse probe (Rand). All metrics are displayed as Mean Values (Standard Deviations).

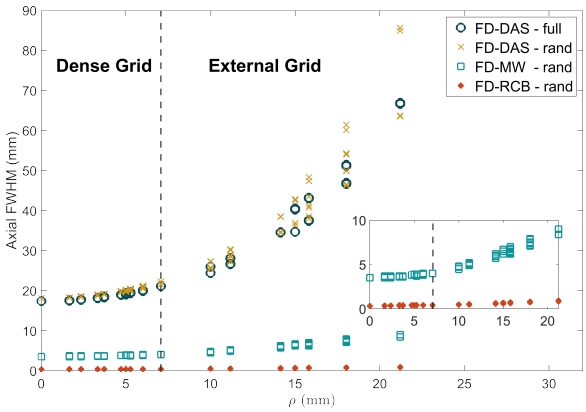

(a)

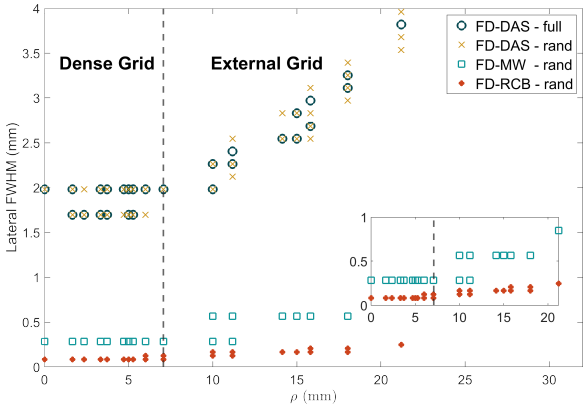

(b)

Fig. 6: [Simulations] (a) Axial and (b) lateral FWHM of the main lobe computed as a function of the distance ρ between the center of the grid at position $(0, 0, 20)$ mm and each point source.

the external part of the displacement grid.

Concerning other metrics, it can be seen, in Table I, there are only minimal differences between the full probe and the sparse random apodization. On the other hand, the use of adaptive beamformers offers considerable improvements for both the PSRL and the imSNR of the reconstructed maps.

C. Harmonic compact scatterer Experiments - Influence of the position of the source

As for simulated data, a presentation of the imaging results for the SNR $= 10\,\mathrm{dB}$ data series is given in Fig. 5.(b-d), which collates sections in the $z = 20.7\,\mathrm{mm}$ plane, of the $-6\,\mathrm{dB}$ main lobes of power maps reconstructed for the needle tip successively placed at every node of the grid, with each of the 3 beamformers above-mentioned. The value $z = 20.7\,\mathrm{mm}$ corresponds to the average tip depth measured on GT images. Points of the external grid with $x < 0$ are not shown because for those positions, the matrix probes intercepted direct emission from the lower part of the HIFU transducer surface, giving rise to a strong interfering source. However, due to the symmetries of the matrix probe, the missing points should provide results similar to points from the $x > 0$ half-plane. As for simulated data, lobe sections are well centered on the nodes of the displacement grid, and their size increases with ρ, due to both an increase of the volume of the main lobe itself and to the tilt of the main lobes. Fig. 5.(a, b) provide a direct comparison of the results for simulation and experiment with FD-DAS beamformer, and show very similar patterns. Fig. 5.(c, d) illustrate the point in using adaptive FD-MW or FD-RCB beamformers to drastically reduce the main lobe sizes. The computation times required to obtain the part of the experimental maps of Fig. 3.(b-d) corresponding to the source at position $(0, 0)$ (composed of 40401 pixels) are respectively $0.50\,\mathrm{s}$ for FD-DAS, $0.55\,\mathrm{s}$ for FD-MW and $270\,\mathrm{s}$ for FD-RCB, which illustrates the high computational cost of the RCB beamformer in comparison to either FD-DAS or FD-MW.

Quantitative analysis is given in Fig. 7 and Table II. Position errors are given in Table II for the SNR $= 10\,\mathrm{dB}$ and SNR $= 2.7\,\mathrm{dB}$ data series. For each SNR value, a first set of metrics gives the mean values with standard deviations over the probe footprint (inner dense grid). Because of the large variations of the metrics over the external grid, only values for points closest to $\rho = 2D$ (shaded area in Fig. 7) are provided in a second set, for comparison with the probe footprint. Position errors are equivalent for all beamformers, around $0.5\,\mathrm{mm}$ for the SNR $= 10\,\mathrm{dB}$ series, and around $1\,\mathrm{mm}$ when SNR is decreased to $2.7\,\mathrm{dB}$, in the probe footprint. For $\rho \sim 2D$, it reaches $2\,\mathrm{mm}$ whatever the beamformer used, for both SNR $= 10\,\mathrm{dB}$ and SNR $= 2.7\,\mathrm{dB}$ series.

The evolution of the axial and lateral FWHM are given as a function of ρ in Fig. 7. As for simulations, variations of

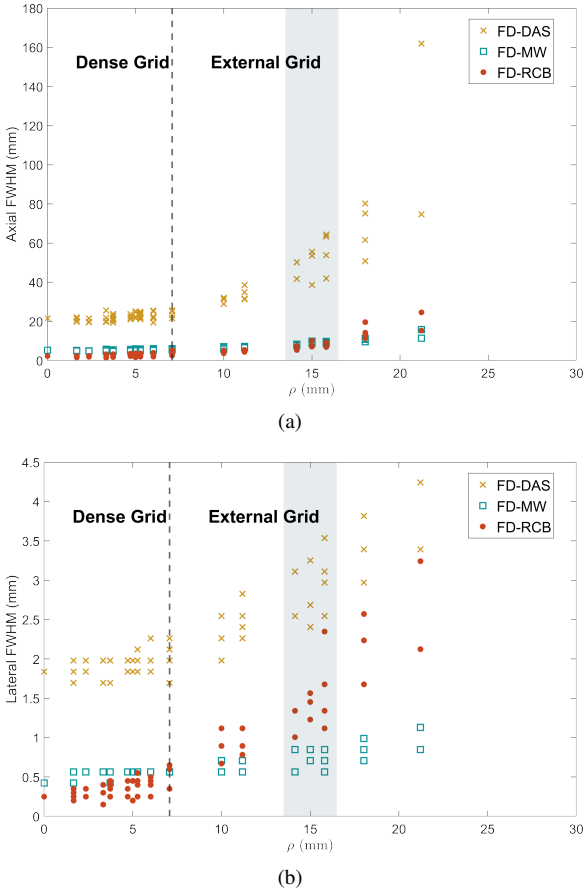

Fig. 7: [Experiments] (a) Axial and (b) lateral FWHM of the main lobe computed as a function of the distance ρ for an SNR $= 10\,\mathrm{dB}$.

the main lobe dimensions are very low for sources in the probe footprint, but as soon as ρ goes beyond D, a clear increase of those metrics can be observed. Table II summarizes those results. For sources in the probe footprint, and for the SNR $= 10\,\mathrm{dB}$ data series, axial FWHM is $22\,\mathrm{mm}$ for FD-DAS beamformer and $5\,\mathrm{mm}$ for FD-MW beamformer, values that are comparable to the one obtained in simulations. For FD-RCB beamformer, it reaches $3\,\mathrm{mm}$, more than 7 times higher than for the simulated data. When SNR is decreased to $2.7\,\mathrm{dB}$, it reaches $7\,\mathrm{mm}$ which is identical to FD-MW beamformer axial FWHM in the same conditions. As expected, lateral FWHM are smaller than axial FWHM, with roughly a factor 15 between both metrics, but similar observations can be done for what concerns the comparison to simulation results or the sensitivity of FD-RCB beamformer to noise level.

Concerning PSLR and imSNR results, if both adaptive beamformers offer very large improvement of the metrics, the striking point is that, for real experiments, FD-MW offers the best performances in all cases, due to a much lower sensitivity to noise level than FD-RCB.

D. Experimental application - Cavitation source

3D maps of the cavitating source placed at position $(3.33, -1.67)\,\mathrm{mm}$ on the displacement grid are shown on Fig. 8 for three reconstruction frequencies. Adaptive FD-MW beamformer is used here for reconstruction, but metrics characterizing the main lobe can be found for the three beamformers in Table III. The lowest reconstruction frequency, $2\,\mathrm{MHz}$, is the same as for the harmonic compact scatterer experiments. It is the first harmonic of the $1\,\mathrm{MHz}$ main component of the emitted burst, and it enables a direct comparison of the metrics between both experiments. As shown in Table III, the position of the cavitating source is identified with a precision similar to harmonic source experiments. Other metrics are similar to the one obtained for the SNR $= 10\,\mathrm{dB}$ series of the harmonic compact scatterer or better. The presence of a small cavitation cloud at the needle tip was confirmed by the ombroscopic imaging performed using the fast optical camera as it can be seen on Fig. 1. Nevertheless, it has to be noted that the $2\,\mathrm{MHz}$ frequency component is generated by the nonlinear dynamics of bubbles as well as by the nonlinear propagation of the HIFU beam exciting bubbles. For that reason, it cannot really attest that the localized source corresponds to cavitation activity. Reconstruction frequencies of $3.5\,\mathrm{MHz}$ and $4.7\,\mathrm{MHz}$ respectively correspond to ultra-harmonics of the excitation signal and to wideband emission, which are both signatures of the presence of cavitation. Main lobes at these frequencies are located at the same position as for the $2\,\mathrm{MHz}$ frequency component, and their size decreases when reconstruction frequency increases. These results illustrate the pertinence of this 3D-PAM approach combining adaptive beamforming with the use of a random sparse matrix, for 3D cavitation imaging.

E. Simulations - Sources on all grid nodes emitting simultaneously

To illustrate the point of using adaptive beamformers in a more complex situation, power maps in the lateral plane $z = 20\,\mathrm{mm}$ with simulated sources on all grid nodes emitting simultaneously are provided in Fig. 9 for FD-DAS, FD-MW and FD-RCB beamformers. The reconstruction frequency is the same as in single source study ($2\,\mathrm{MHz}$) for the sake of comparison, even if a higher frequency could be used here since sources are emitting wideband signal, as explained in section III-B. It is clear that, for the FD-DAS beamformer, sources in the dense grid cannot be reliably recovered: Some maxima are ill-positioned and sources along the $x-$ direction are poorly separated. In the less dense external grid, sources can be recovered and separated, but with a poor contrast. For the adaptive beamformers, the situation is better, and sources can be recovered either in the inner dense grid or in the external grid.

An average gap between sources can be evaluated by taking the difference between average values of the map on the grid nodes and on the positions between nodes either in the $x-$ or in the $y-$ directions. In the case of the FD-DAS beamformer, this gap is only $\sim 6\,\mathrm{dB}$ in the external grid and 0.3 (resp. 1.5) dB in the $x-$ (resp. $y-$) direction in the inner grid. Moreover, local maxima of the power map are often ill-positionned along the $x-$direction, giving wrong positions of the sources. The difference between $x-$ and $y-$ directions that can also be seen for the other beamformers, is due to

	Position Error (mm)	Axial FWHM (mm)	Lateral FWHM (mm)	PSLR (dB)	Axial ImSNR (dB)	Lateral imSNR (dB)
SNR $= 10\,\mathrm{dB}$						
Dense Grid						
FD-DAS	0.5 (0.3)	22 (4)	1.9 (0.1)	−9 (1)	8.2 (0.2)	15.6 (0.4)
FD-MW	0.4 (0.2)	5 (1)	0.6 (0.1)	−50 (8)	14.2 (0.3)	44 (2)
FD-RCB	0.4 (0.2)	3 (1)	0.4 (0.1)	−34 (7)	18 (2)	42 (7)
$\rho \simeq 2D$						
FD-DAS	2 (1)	50 (10)	2.9 (0.4)	−8 (1)	8.5 (0.6)	13.1 (0.4)
FD-MW	2 (1)	9 (1)	0.8 (0.1)	−50 (6)	11.1 (0.3)	30 (2)
FD-RCB	2 (1)	8 (1)	1.4 (0.4)	−21 (3)	12 (1)	29 (3)
SNR $= 2.7\,\mathrm{dB}$						
Dense Grid						
FD-DAS	2 (1)	26 (8)	2.1 (0.2)	−7 (2)	9.2 (0.5)	14.6 (0.6)
FD-MW	1.0 (0.4)	7 (1)	0.6 (0.1)	−30 (5)	14.6 (0.4)	32 (2)
FD-RCB	0.8 (0.4)	7 (1)	1.2 (0.2)	−14 (2)	13 (1)	22 (2)
$\rho \simeq 2D$						
FD-DAS	2 (2)	50 (20)	3.0 (0.5)	−7 (1)	7.4 (0.7)	13.0 (0.7)
FD-MW	2 (1)	10 (2)	0.8 (0.1)	−37 (8)	12.8 (0.6)	29 (3)
FD-RCB	2 (1)	14 (6)	2.0 (0.5)	−12 (4)	10 (1)	19 (2)

TABLE II: [Experiments] Position errors, FWHM and imSNR in the axial and lateral directions, as well as PSLR in the dense grid and for points with $\rho \simeq 2D$ (highlighted portion of the external grid in Fig. 7). The values account for FD-DAS, FD-MW and FD-RCB on experimental measurements where SNR $= 10\,\mathrm{dB}$ on the top part of the table and SNR $= 2.7\,\mathrm{dB}$ on the bottom part. All metrics are displayed as Mean Values (Standard Deviations).

the small asymmetry of the probe mentioned above, and is consistent with the slightly larger aperture in the $y-$ direction than in the $x-$ direction. For the FD-MW beamformer, the gap is $\geq 25\,\mathrm{dB}$ for the external grid, and 2.5 (resp. 8.5) dB in the $x-$ (resp. $y-$) direction in the inner grid, which enables to recover and separate all sources, with position errors always lower than $0.2\,\mathrm{mm}$. For the FD-RCB beamformer, two ϵ values are provided: $\epsilon = 0.1$ corresponds to the value used in Fig. 5, but does not enable here to recover at a level higher than $-10\,\mathrm{dB}$ all sources in the external grid, and $\epsilon = 10$, which best recovers all sources. In that case, the gap is $\geq 30\,\mathrm{dB}$ for the external grid, and 8 (resp. 19) dB in the $x-$ (resp. $y-$) direction in the inner grid. Sources are clearly recovered, with position errors smaller than $0.1\,\mathrm{mm}$.

V. Discussion

In this study, simulations and experiments have been performed to achieve 3D passive cavitation imaging with reduced PSF sizes using a commercial matrix array and a 256-channel research platform. For that purpose a method based on Fourier domain adaptive beamforming combined with random sparse apodization has been proposed and evaluated. Simulations and experiments have been performed with a harmonic source placed at a given depth but with different distances ρ to the probe axis. The position errors and the FWHM in the axial and lateral dimensions have been evaluated with respect to the distance ρ for different algorithms and apodizations. An additional experimental application on a cavitation source has been performed to assess the beamformer performances at different frequencies on a real cavitation signal. A multi-source configuration has also been provided to illustrate how the beamformers perform in a more complex situation. Considering the good agreement between results for experimental and simulated configurations, the proposed configuration is a simulation with sources on all grid nodes emitting simultaneously, which offers the advantage of enabling direct comparison with single source results. Note that, for this multi-source configuration, wideband random noise emission had to be used in order to reduce the coherence between sources, TEA-based beamformers assuming it to be zero.

The relevance of the use of random sparse apodization was confirmed by the simulations comparing FD-DAS mapping obtained with the full and the random sparse probe. In a similar configuration, Therre *et al.* [22] provided indications that using a reduced number of elements does not decrease the image quality of the cavitation mapping. Before this study, sparse arrays had already been used to build large aperture custom-built arrays for 3D-PAM with elements distributed over hemispherical or spherically-curved surfaces [16]–[21]. In the context of therapy, Goss *et al.* [36] however noticed a performance decrease in the case of an off-axis focusing. Our simulations over the whole grid showed that full and random sparse probes had a similar evolution as a function of ρ (Fig. 6), despite the fact that using a random sparse apodization slightly increases the dispersion on the metrics for a given distance. In fact, it introduces some irregularity on the secondary lobes which can be seen as a rise of the background noise at an acceptable level of $\simeq -15$ dB (Fig. 3). Hence, while reducing the computation cost and making the application more manageable with a single 256-channel US scanner, the image quality is not affected.

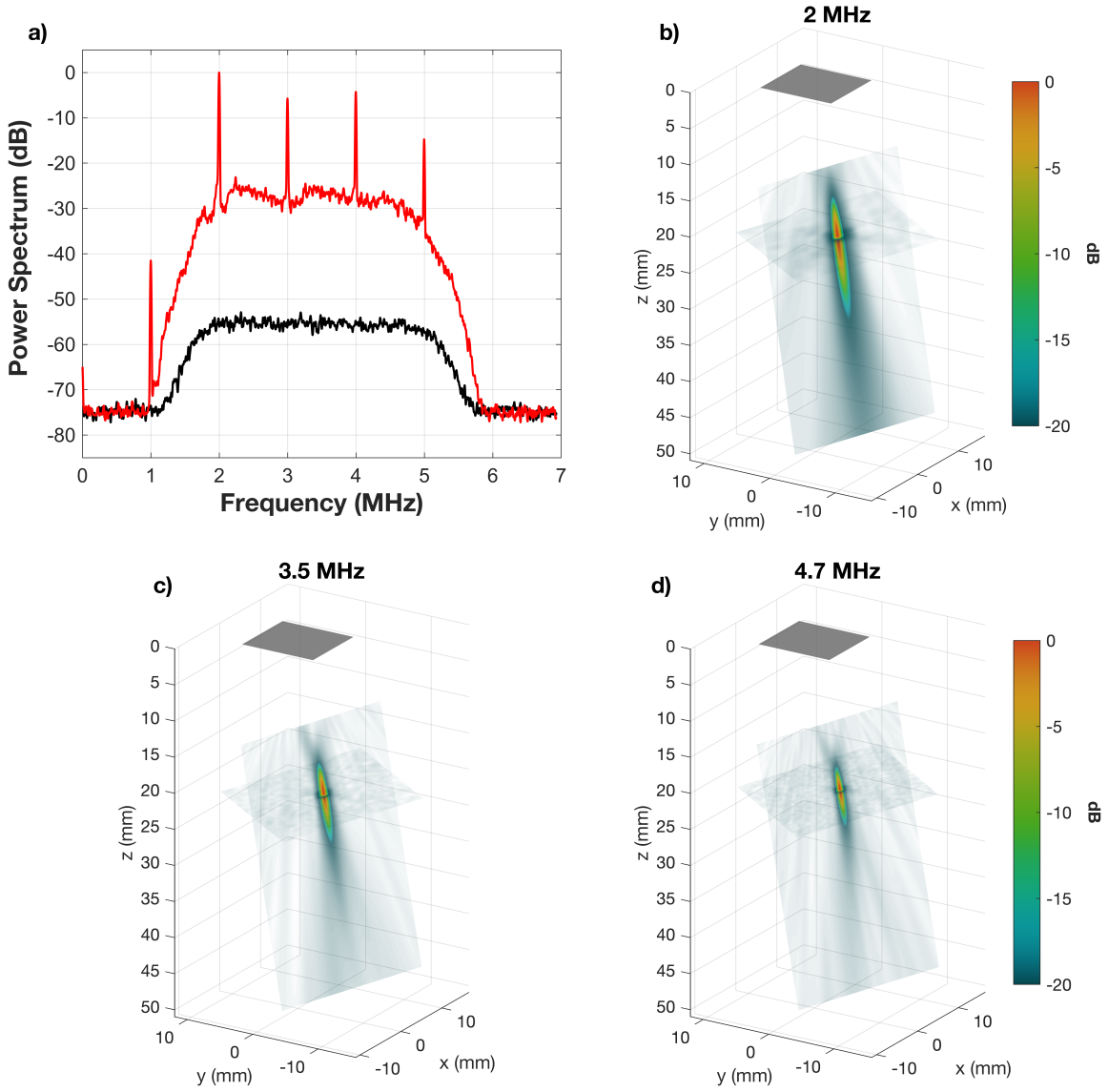

Fig. 8: 3D visualization of axial and lateral plane sections of a cavitation source reconstructed with FD-MW at 3 different frequencies: (b) a harmonic frequency at $2\,\mathrm{MHz}$, (c) an ultra-harmonic frequency at $3.5\,\mathrm{MHz}$ and (d) an arbitrary frequency different from the previous cases at $4.7\,\mathrm{MHz}$. The frequency spectrum of a typical signal is presented in (a) (red curve), the black curve corresponding to a spectrum without HIFU emission.

The results shown in Section IV show different situations when the source is inside the probe footprint (dense grid) or outside the probe footprint (external grid). Inside the probe footprint, the position errors are not significant in simulations, and lower than the lateral FWHM in harmonic compact scatterer experiments for all beamformers, reaching $\simeq 0.5\,\mathrm{mm}$ for the SNR $= 10\,\mathrm{dB}$ series, and $\simeq 1\,\mathrm{mm}$ for the SNR $= 2.7\,\mathrm{dB}$ series (see Table II). It is even lower in the cavitating source experiments, with values reaching $0.2 - 0.4\,\mathrm{mm}$ regardless of the beamformer used and of the frequency chosen for the mapping.

Concerning main lobe sizes, the use of adaptive beamformers allows to largely reduce both axial and lateral FWHM. For simulations, Table I shows that the FD-DAS axial FWHM is reduced by a factor $\simeq 5$ when FD-MW is used instead, and by a factor $\simeq 50$ for FD-RCB with an optimal value of ϵ. Of course, such values are not reached in experiments, but using FD-MW results in a $\simeq 4$ reduction of the axial FWHM in Table II. For FD-RCB, performances strongly depend on the noise level in the acquisition signals, since the axial FWHM is still $\simeq 8$ times lower than for the FD-DAS beamformer for the SNR $= 10\,\mathrm{dB}$ series, but is only 3.7 times lower for the SNR $= 2.7\,\mathrm{dB}$ series, not better than FD-MW.

The results for the PSLR and for either the axial or lateral imSNR also show a large enhancement of the reconstructed maps when an adaptive beamformer is used: For example, for harmonic compact scatterer experiments with the lowest SNR, Table II shows that FD-MW still enables a $20\,\mathrm{dB}$ reduction

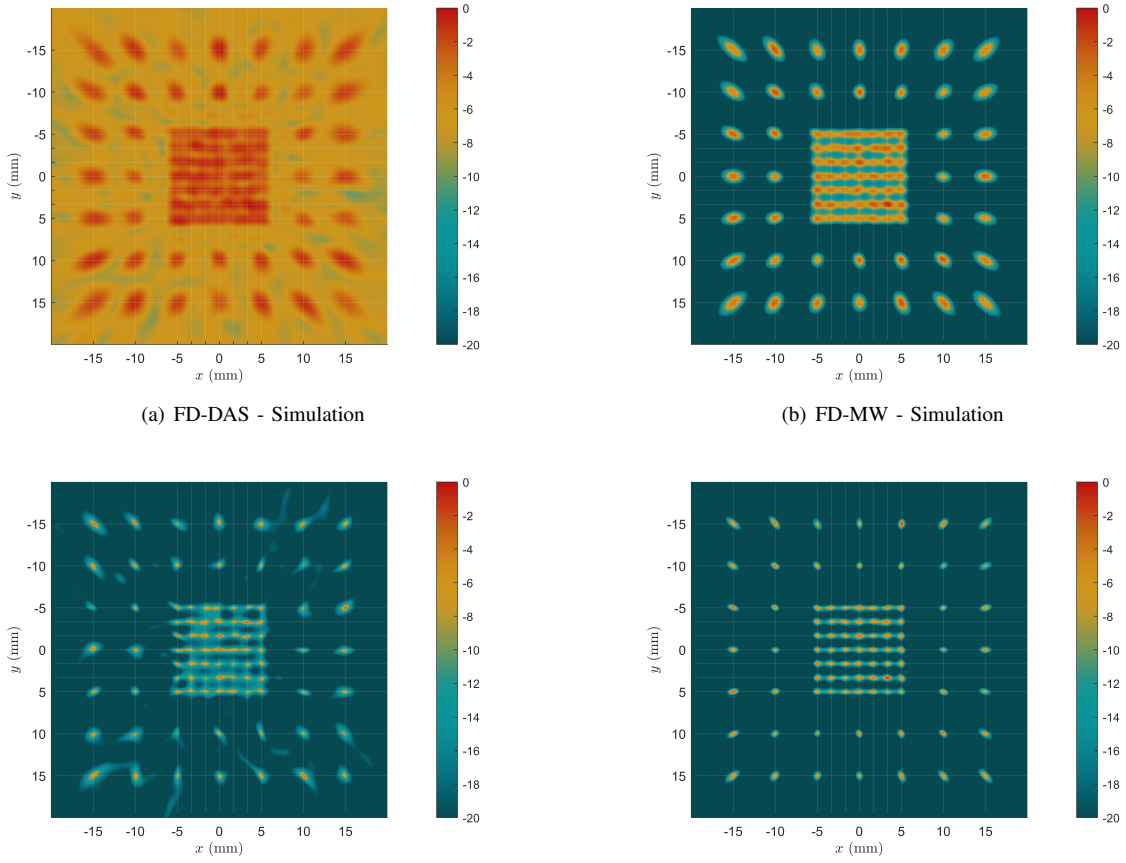

(a) FD-DAS - Simulation

(b) FD-MW - Simulation

(c) FD-RCB ($\epsilon = 0.1$) - Simulation

(d) FD-RCB ($\epsilon = 10$) - Simulation

Fig. 9: PAM in the lateral plane $z = 20\,\mathrm{mm}$ with simulated sources on all grid nodes emitting wideband noise simultaneously (a) with FD-DAS, (b) FD-MW, (c) FD-RCB ($\epsilon = 0.1$) and (d) FD-RCB ($\epsilon = 10$) beamformers, respectively. Ground Truth is simply given by the nodes of the grid drawn on the power map for the sake of clarity of the plots.

of the PSLR in comparison to FD-DAS ; For the cavitation experiments (Table III), the gain is even larger and reaches $62\,\mathrm{dB}$ for the $2\,\mathrm{MHz}$ reconstruction frequency, and $44\,\mathrm{dB}$ for the $4.7\,\mathrm{MHz}$ reconstruction frequency. The sensitivity of FD-RCB to the noise level is also illustrated more clearly on these metrics, since FD-MW offers the best performances for all experimental results in Tables II and III.

While the main lobe sizes are almost unchanged when the source is inside the probe footprint for all beamformers, they increase rapidly when the distance from the source to the probe axis goes beyond D. This point is also observed for the dispersion of the measurements at a given distance ρ. Such a degradation of performances outside the probe footprint is not specific from the passive mapping, since it is also observed for active US imaging, as already mentioned in Section III-C. Nevertheless, even for the distance $\rho \simeq 2D$ highlighted in Fig. 7 and Table II, axial and lateral FWHM of both adaptive beamformers are still much better than the ones of FD-DAS inside the probe footprint, which makes possible the use of 3D-PAM even in that region. Here again, it can be noted that for the SNR $= 2.7\,\mathrm{dB}$ series, outside the probe footprint, FD-RCB performances are degraded, and in that conditions, FD-MW offers the best metrics. Even if FD-RCB metrics could be slightly enhanced with a specific optimization of the ϵ value for each measurement, this points out the sensitivity of RCB performances to the noise level in the acquired signals.

These results illustrate the benefit of using adaptive beamformers instead of the non-adaptive DAS algorithm: If the latter is adequate and gives reasonably good performances for low f-number configurations, which can be the case for 2D-PAM where large aperture linear probes are commonly used, or in specific configurations as discussed above, it turns out to be inadequate for 3D-PAM with matrix arrays of small aperture because of the strong impact of the diffraction pattern of the array in that case. At first sight, FD-RCB offers the best performances but it has to be noted that its metrics are strongly deteriorated in the case of experimental noisy signals. Two aspects could take part in this degradation: First, the complexity of the algorithm itself, with its matrix inversion and its optimization step, could be an element that would make FD-RCB more sensitive to noise level than more basic DAS-based beamformers, as seen on the metrics obtained respectively with the SNR $= 10\,\mathrm{dB}$ and SNR $= 2.7\,\mathrm{dB}$ experiments, in Table II. A second element that could have to be taken into account is

	Position Error (mm)	Axial FWHM (mm)	Lateral FWHM (mm)	PSLR (dB)	Axial ImSNR (dB)	Lateral imSNR (dB)
			2 MHz			
FD-DAS	0.4 (0.4)	23 (1)	1.5 (0.1)	−8.8 (0.2)	9.7 (0.2)	15.5 (0.3)
FD-MW	0.3 (0.1)	5.8 (0.3)	0.6 (0.1)	−71 (3)	13.5 (0.2)	28 (2)
FD-RCB	1 (0.1)	2.5 (0.2)	0.5 (0.1)	−78 (2)	12.3 (0.4)	22 (1)
			3.5 MHz			
FD-DAS	0.3 (0.1)	11.3 (0.5)	0.9 (0.1)	−8 (1)	12.2 (0.2)	17.2 (0.2)
FD-MW	0.2 (0.1)	4.1 (0.2)	0.5 (0.1)	−57 (3)	14.8 (0.2)	23 (1)
FD-RCB	1.4 (0.2)	2.1 (0.2)	0.4 (0.1)	−59 (5)	13.8 (0.4)	24 (2)
			4.7 MHz			
FD-DAS	0.3 (0.1)	8 (1)	0.7 (0.1)	−7 (1)	13.4 (0.3)	17.7 (0.2)
FD-MW	0.3 (0.1)	3.1 (0.2)	0.4 (0.1)	−51 (3)	15.9 (0.2)	22 (1)
FD-RCB	2 (0.3)	1.5 (0.5)	0.4 (0.1)	−36 (8)	15 (1)	24 (3)

TABLE III: Position errors, FWHM and imSNR in the axial and lateral directions, as well as PSLR of the cavitation maps at theoretical position $(3.33, -1.67)$. The values account for FD-DAS, FD-MW and FD-RCB. All metrics are displayed as Mean Values (Standard Deviations) over a set of 27 cavitation signal recordings realized in the same configuration.

that, when going from simulations to real experimental signals, both with SNR $= 10\,\mathrm{dB}$, larger ϵ values have to be chosen to take larger model errors into account, which could be responsible for an increase of the PSF size, and of a deterioration of the PSLR and the imSNR of the maps. Considering the fact that in real in vivo experiments, model errors would be even higher than in the idealized experimental context used here, higher ϵ values would have to be used, making FD-MW a better choice, like in the case of the SNR $= 2.7\,\mathrm{dB}$ experiments presented here. Together with the fact that the 3D mapping involves a large number of reconstruction pixels, having to find the optimal ϵ is a heavy constraint which increases even more an already high computational cost of this beamformer, which seems to preclude the use of RCB for 3D-PAM. Regarding FD-MW, it offers a large improvement of the metrics in comparison to FD-DAS, but with a computational cost close to the one of FD-DAS, which places it as a good compromise to enhance performances of 3D-PAM.

The simulated configuration with sources on all grid nodes emitting simultaneously demonstrates the efficiency of the adaptive algorithms in comparison to the non-adaptive FD-DAS beamformer, to identify and separate multiple sources in a rather complex situation. Again, FD-RCB offers the best performances, provided that ϵ value is well-chosen: In Fig. 9.c, with $\epsilon = 0.1$ that was well adapted for sinusoidal sources of Fig. 5, few sources appear to have a level below $-12\,\mathrm{dB}$ and are thus completely lost, while an $\epsilon = 10$ value (Fig. 9.d) enables to recover and separate all sources, with gaps between sources larger than $8\,\mathrm{dB}$ even in the dense grid, and position errors lower than $0.1\,\mathrm{mm}$. As before, in view of the constraint of the necessary ϵ value optimization, FD-MW can be seen as a good compromise: It recovers and separates all the sources, with average gaps of 2.5 and 8.5 dB in the $x-$ and $y-$ directions respectively, and a position error lower than $0.2\,\mathrm{mm}$, while having a computational cost equivalent to the one of FD-DAS, and no adaptive parameter to optimize. Interestingly, these results are consistent with the metrics given for single source experiments: With its lateral FWHM larger than $1.5\,\mathrm{mm}$, FD-DAS cannot isolate $1.6\,\mathrm{mm}$-separated sources in the dense grid ; FD-MW and FD-RCB can do it with their respective lateral FWHM of 0.6 and $0.4\,\mathrm{mm}$, and the position error, always lower than $0.2\,\mathrm{mm}$, is fully coherent with the single source value given in Table III (taken here as a reference since sources are emitting wideband noise).

Real cavitation events have also been imaged passively, and the results given in Table III for a reconstruction frequency of $2\mathrm{MHz}$ are comparable to the ones obtained with the harmonic compact scatterer for the SNR $= 10\,\mathrm{dB}$ series. For higher reconstruction frequencies of $3.5\mathrm{MHz}$ and $4.7\mathrm{MHz}$, main lobe dimensions decrease with the wavelength for the FD-DAS beamformer. However, the decrease is less pronounced for both adaptive beamformers, for which the lobe dimensions approach the real size of the bubble cloud, $\lesssim 0.5\,\mathrm{mm}$ according to optical images of the cloud. It has to be noted that, in the harmonic compact scatterer experiments, the reconstruction of the power maps at those frequencies did not show any source, confirming the absence of cavitation in those experimental configurations. 3D-PAM using a random sparse array and Fourier domain adaptive algorithms can thus be used for cavitation imaging, with the advantage of the Fourier domain analysis, which enables to discriminate between cavitating and non-cavitating sources and between stable cavitation and collapsing bubbles.

It has to be underlined that all the results presented here correspond to a relatively shallow source depth of $20\,\mathrm{mm}$. This choice was guided by the constraint of working with generic commercial probes whose aperture size is only $1\,\mathrm{cm}$: As a matter of fact, for this aperture size, a simulation in the same configuration as in Section IV-A, but with a source placed at a depth of $60\,\mathrm{mm}$, results in an axial FWHM larger than $500\,\mathrm{mm}$ for the FD-DAS beamformer, which questions the pertinence of a comparison with other beamformers at this depth. Nevertheless, it was checked that, even at this depth, there is a qualitative similarity of the results with the ones obtained at $20\,\mathrm{mm}$. In particular, it was checked that the full probe and the random sparse probe configurations give

similar power maps, and that the benefit of using adaptive beamformers is conserved. But it has to be kept in mind that quantitative results and relative comparison between algorithms may vary. For example, in the simulated $60\,\mathrm{mm}$ configuration mentioned above, axial FWHM is around $40\,\mathrm{mm}$ for the FD-MW beamformer and $4\,\mathrm{mm}$ for the FD-RCB beamformer, respectively more than 12 times and 120 times smaller than for the FD-DAS beamformer, while the ratio is respectively 5.3 and 50 for the $20\,\mathrm{mm}$ configuration, according to Table I.

Recent studies already performed 3D-PAM using Time Domain DAS beamforming and either commercial or custom imaging probes. Custom hemispherical sparse arrays designed for skull therapy monitoring has been used in [16]–[19] or in [20]. For that specific application, a sparse hemispherical phased array has been used to provide a very large aperture array of $\simeq 30\,\mathrm{cm}$ in diameter. Thanks to this large aperture, a non-adaptive DAS beamforming was sufficient to achieve 3D-PAM with a FWHM in any direction of about $4\,\mathrm{mm}$. Values of PSLR and imSNR reported in [16] are, at best, $-11\,\mathrm{dB}$ and $23\,\mathrm{dB}$ respectively for the full 1372-element array. Comparable results were obtained by Liu *et al.* [21] who used a sparse distribution of receiving elements in a custom-made spherically-curved dual-mode array with an f-number of 0.83, also designed for transcranial therapy. In another study, Escudero *et al.* [13] used a more versatile commercial imaging probe identical to the one used in this paper, driven by four synchronized Vantage systems in order to make use of the 1024 channels simultaneously. With a Singular-Value Decomposition method for moving tissue imaging, they took advantage of the short number of cycles in each pulse to improve the image quality, especially in the axial dimension, which reduces the versatility of the method. The cavitation cloud nucleated with a peak negative pressure of 8 to $9\,\mathrm{MPa}$ in the focal zone resulted in a $\simeq 10\,\mathrm{mm}$ main lobe FWHM in both directions at a distance of $140\,\mathrm{mm}$ from the probe. With the same commercial Vermon probe driven by a 1024-channel ultrasound research platform, Therre *et al.* [22] performed a 3D mapping with DAS beamforming of a cavitating source at a distance of $60\,\mathrm{mm}$ from the probe. Under these circumstances, the main lobe axial FWHM is more than $50\,\mathrm{mm}$ because of the large observation distance. To recover an axial FWHM lower than $10\,\mathrm{mm}$, a custom-made probe with an aperture three times larger than the Vermon probe had to be used. In that context, the methods proposed in this paper, combining random sparse apodization with adaptive beamforming, enable to obtain an axial FWHM of $5\,\mathrm{mm}$ or less with a commercial probe of small aperture and one single 256-channel ultrasound research platform. Among adaptive beamformers proposed here, FD-RCB suffers from its high computation cost, while FD-MW, with its low complexity close to the one of FD-DAS, provides a compromise between performances and computation time which is particularly interesting for 3D passive cavitation imaging.

VI. Conclusion

In this paper, we have proposed and evaluated the use of random sparse arrays and adaptive beamformers for 3D-PAM. The evaluation was made both in simulations and experiments with a systematic analysis. A harmonic source has been placed on nodes of a grid in the plane normal to the probe axis $20\,\mathrm{mm}$ away from the probe, in order to evaluate the position errors, the PSLR, as well as the axial and lateral FWHM and imSNR. It showed the interest of using adaptive algorithms, in particular FD-MW, to reduce the dimensions of the main lobes and enhance image quality while keeping a reasonable computation time. FD-RCB proved to be very sensitive to noise level with an ϵ parameter that would need to be optimized for each condition in order to get optimal performances. In addition, when compared to the full array, the use of a random sparse probe only induced minor differences on the noise level of the 3D mapping, with however no degradation of the metrics. Finally, the 3D mapping of a real cavitation source presented performances comparable to the high SNR series of the harmonic source experiments for a $2\,\mathrm{MHz}$ reconstruction frequency, and it has been checked that with a reconstruction frequency corresponding to an ultra-harmonic of the HIFU signal or to wideband noise the cavitation source could be localized, while no source was imaged at such frequencies for harmonic source experiments. These results show that the proposed method, combining a random sparse apodization with adaptive beamforming, enables to achieve high-performance 3D-PAM with a manageable device involving a commercial probe of small aperture driven by a single 256-channel ultrasound research platform.

Acknowledgments

This work was supported by the ANR project CAVIIAR (ANR-22-CE19-0006), the LABEX CELYA (ANR-11-LABX-0060) and performed within the framework of the LABEX PRIMES (ANR-11-LABX-0063) of Université de Lyon, within the program "Investissements d'Avenir" (ANR-11-IDEX-0007) operated by the French National Research Agency (ANR).

References

[1] K. Kooiman, S. Roovers, S. A. Langeveld, R. T. Kleven, H. Dewitte, M. A. O'Reilly, J.-M. Escoffre, A. Bouakaz, M. D. Verweij, K. Hynynen *et al.*, "Ultrasound-responsive cavitation nuclei for therapy and drug delivery," *Ultrasound in medicine & biology*, vol. 46, no. 6, pp. 1296–1325, 2020.

[2] V. A. Khokhlova, J. B. Fowlkes, W. W. Roberts, G. R. Schade, Z. Xu, T. D. Khokhlova, T. L. Hall, A. D. Maxwell, Y.-N. Wang, and C. A. Cain, "Histotripsy methods in mechanical disintegration of tissue: Towards clinical applications," *International journal of hyperthermia*, vol. 31, no. 2, pp. 145–162, 2015.

[3] L. Arnold, A. Hendricks-Wenger, S. Coutermarsh-Ott, J. Gannon, A. N. Hay, N. Dervisis, S. Klahn, I. C. Allen, J. Tuohy, and E. Vlaisavljevich, "Histotripsy ablation of bone tumors: Feasibility study in excised canine osteosarcoma tumors," *Ultrasound in Medicine & Biology*, 2021.

[4] M. Marinova, M. Rauch, M. Mücke, R. Rolke, M. A. Gonzalez-Carmona, J. Henseler, H. Cuhls, L. Radbruch, C. P. Strassburg, L. Zhang *et al.*, "High-intensity focused ultrasound (hifu) for pancreatic carcinoma: evaluation of feasibility, reduction of tumour volume and pain intensity," *European radiology*, vol. 26, no. 11, pp. 4047–4056, 2016.

[5] H. Zhong, H. Hu, C. Bai, R. Liu, J. Wan, and M. Wan, "Cavitation imaging in tissues," in *Cavitation in Biomedicine, Principles and Techniques*. Springer, 2015, ch. 7, pp. 331–399.

[6] T. Ding, H. Yin, H. Hu, C. Bai, and M. Wan, "Cavitation mapping," in *Cavitation in Biomedicine, Principles and Techniques*. Springer, 2015, ch. 2, pp. 47–114.

[7] N. R. Owen, M. R. Bailey, and L. A. Crum, "A method to synchronize high-intensity, focused ultrasound with an arbitrary ultrasound imager," *IEEE transactions on ultrasonics, ferroelectrics, and frequency control*, vol. 53, no. 3, pp. 645–650, 2006.

[8] M. Gyongy and C.-C. Coussios, "Passive spatial mapping of inertial cavitation during hifu exposure," *IEEE Transactions on Biomedical Engineering*, vol. 57, no. 1, pp. 48–56, 2009.

[9] C. Coviello, R. Kozick, J. Choi, M. Gyöngy, C. Jensen, P. P. Smith, and C.-C. Coussios, "Passive acoustic mapping utilizing optimal beamforming in ultrasound therapy monitoring," *The Journal of the Acoustical Society of America*, vol. 137, no. 5, pp. 2573–2585, 2015.

[10] P. Stoica, Z. Wang, and J. Li, "Robust capon beamforming," in *Conference Record of the Thirty-Sixth Asilomar Conference on Signals, Systems and Computers, 2002.*, vol. 1. IEEE, 2002, pp. 876–880.

[11] J. Li, P. Stoica, and Z. Wang, "On robust capon beamforming and diagonal loading," *IEEE transactions on signal processing*, vol. 51, no. 7, pp. 1702–1715, 2003.

[12] P. Boulos, F. Varray, A. Poizat, A. Ramalli, B. Gilles, J.-C. Bera, and C. Cachard, "Weighting the passive acoustic mapping technique with the phase coherence factor for passive ultrasound imaging of ultrasound-induced cavitation," *IEEE transactions on ultrasonics, ferroelectrics, and frequency control*, vol. 65, no. 12, pp. 2301–2310, 2018.

[13] D. S. Escudero, G. Goudot, M. Vion, M. Tanter, and M. Pernot, "2d and 3d real-time passive cavitation imaging of pulsed cavitation ultrasound therapy in moving tissues," *Physics in Medicine & Biology*, vol. 63, no. 23, p. 235028, 2018.

[14] A. Fenster, D. B. Downey, and H. N. Cardinal, "Three-dimensional ultrasound imaging," *Physics in medicine & biology*, vol. 46, no. 5, p. R67, 2001.

[15] Q. Huang and Z. Zeng, "A review on real-time 3d ultrasound imaging technology," *BioMed research international*, vol. 2017, 2017.

[16] R. M. Jones, M. A. O'Reilly, and K. Hynynen, "Transcranial passive acoustic mapping with hemispherical sparse arrays using CT-based skull-specific aberration corrections: a simulation study," *Physics in Medicine and Biology*, vol. 58, no. 14, pp. 4981–5005, 2013.

[17] M. A. O'Reilly, R. M. Jones, and K. Hynynen, "Three-dimensional transcranial ultrasound imaging of microbubble clouds using a sparse hemispherical array," *IEEE Transactions on Biomedical Engineering*, vol. 61, no. 4, pp. 1285–1294, 2014.

[18] L. Deng, M. A. O'Reilly, R. M. Jones, R. An, and K. Hynynen, "A multi-frequency sparse hemispherical ultrasound phased array for microbubble-mediated transcranial therapy and simultaneous cavitation mapping," *Physics in Medicine & Biology*, vol. 61, no. 24, p. 8476, 2016.

[19] R. M. Jones, L. Deng, K. Leung, D. McMahon, M. A. O'Reilly, and K. Hynynen, "Three-dimensional transcranial microbubble imaging for guiding volumetric ultrasound-mediated blood-brain barrier opening," *Theranostics*, vol. 8, no. 11, pp. 2909–2926, 2018.

[20] C. Crake, S. T. Brinker, C. M. Coviello, M. S. Livingstone, and N. J. McDannold, "A dual-mode hemispherical sparse array for 3d passive acoustic mapping and skull localization within a clinical mri guided focused ultrasound device," *Physics in Medicine & Biology*, vol. 63, no. 6, p. 065008, 2018.

[21] H.-L. Liu, C.-H. Tsai, C.-K. Jan, H.-Y. Chang, S.-M. Huang, M.-L. Li, W. Qiu, and H. Zheng, "Design and implementation of a transmit/receive ultrasound phased array for brain applications," *IEEE Transactions on Ultrasonics, Ferroelectrics, and Frequency Control*, vol. 65, no. 10, pp. 1756–1767, oct 2018.

[22] S. Therre, W. Bost, H. Hewener, S. Tretbar, and M. Fournelle, "Passive acoustic mapping for ultrasound therapy monitoring," *Current Directions in Biomedical Engineering*, vol. 7, no. 2, pp. 437–440, 2021.

[23] S. S. Brunke and G. R. Lockwood, "Broad-bandwidth radiation patterns of sparse two-dimensional vernier arrays," *IEEE transactions on ultrasonics, ferroelectrics, and frequency control*, vol. 44, no. 5, pp. 1101–1109, 1997.

[24] E. Roux, F. Varray, L. Petrusca, C. Cachard, P. Tortoli, and H. Liebgott, "Experimental 3-d ultrasound imaging with 2-d sparse arrays using focused and diverging waves," *Scientific reports*, vol. 8, no. 1, pp. 1–12, 2018.

[25] A. Sivadon, F. Varray, B. Nicolas, J.-C. Béra, and B. Gilles, "Using sparse array for 3d passive cavitation imaging," in *2020 IEEE International Ultrasonics Symposium (IUS)*. IEEE, 2020, pp. 1–4.

[26] S. Lu, X. Yu, R. Li, Y. Zong, and M. Wan, "Passive cavitation mapping using dual apodization with cross-correlation in ultrasound therapy monitoring," *Ultrasonics Sonochemistry*, vol. 54, pp. 18–31, Jun 2019.

[27] M. Polichetti, F. Varray, B. Gilles, J.-C. Béra, and B. Nicolas, "Use of the cross-spectral density matrix for enhanced passive ultrasound imaging of cavitation," *IEEE Transactions on Ultrasonics, Ferroelectrics, and Frequency Control*, vol. 68, no. 4, pp. 910–925, 2020.

[28] D. E. Grant, J. H. Gross, and M. Zebrick Lawrence, "Cross-spectral matrix estimation effects on adaptive beamforming," *The Journal of the Acoustical Society of America*, vol. 98, no. 1, pp. 517–524, 1995.

[29] J. Maksym, "A robust formulation of an optimum cross-spectral beamformer for line arrays," *The Journal of the Acoustical Society of America*, vol. 65, no. 4, pp. 971–975, 1979.

[30] J. Yu, H. Yoon, Y. M. Khalifa, and S. Y. Emelianov, "Design of a volumetric imaging sequence using a vantage-256 ultrasound research platform multiplexed with a 1024-element fully sampled matrix array," *IEEE transactions on ultrasonics, ferroelectrics, and frequency control*, vol. 67, no. 2, pp. 248–257, 2019.

[31] E. Lyka, C. M. Coviello, C. Paverd, M. D. Gray, and C. C. Coussios, "Passive acoustic mapping using data-adaptive beamforming based on higher order statistics," *IEEE transactions on medical imaging*, vol. 37, no. 12, pp. 2582–2592, 2018.

[32] P. Stoica, J. Li, and X. Tan, "On spatial power spectrum and signal estimation using the pisarenko framework," *IEEE Transactions on Signal Processing*, vol. 56, no. 10, pp. 5109–5119, 2008.

[33] L. Du, T. Yardibi, J. Li, and P. Stoica, "Review of user parameter-free robust adaptive beamforming algorithms," *Digital Signal Processing*, vol. 19, no. 4, pp. 567–582, 2009.

[34] A. Sivadon, M. Polichetti, J.-C. Béra, F. Varray, B. Nicolas, and B. Gilles, "Pisarenko class beamformer applied to passive acoustic mapping of ultrasound cavitation," in *Forum Acusticum*, 2020, pp. 1061–1064.

[35] S. Norton and I. Won, "Time exposure acoustics," *IEEE Transactions on Geoscience and Remote Sensing*, vol. 38, no. 3, pp. 1337–1343, May 2000.

[36] S. A. Goss, L. A. Frizzell, J. T. Kouzmanoff, J. M. Barich, and J. M. Yang, "Sparse random ultrasound phased array for focal surgery," *IEEE transactions on ultrasonics, ferroelectrics, and frequency control*, vol. 43, no. 6, pp. 1111–1121, 1996.